Where photons meet phonons

Buters, F.M.

10

Optomechanical experiments in a cryogen free dilution refrigerator

We have shown in the previous chapters how optical cooling can greatly reduce the effective mode temperature of the mechanical resonator. In this chapter, we perform optical side-band cooling at cryogenic temperatures, since only a combination of optical and cryogenic cooling will be sufficient to reach the quantum mechanical ground state. First, we describe the mass-spring system developed to mechanically isolate the optical set-up from the vibrations generated in a cryogen free cryostat. Next we demonstrate how via optical side-band cooling an effective mechanical mode temperature of 3.09 ± 0.07 mK is achieved. This temperature corresponds to an RMS motion of 9.2 ± 0.15 fm, demonstrating femtometer read-out precision in a dry cryostat. Finally we discuss some of the limiting factors in achieving the quantum mechanical ground-state and suggest improvements for the future.

10.1 Mechanical low-pass filters

The experiments at cryogenic temperatures are performed in a cryogen free dilution refrigerator (Leiden Cryogenics CF-CS81-1400) which uses a pulse tube (PT) cryocooler instead of liquid helium to reach 4 Kelvin. The use of a cryocooler introduces additional vibrations, from which the experiment needs to be isolated. The cryostat itself is already modified to reduce vibrations. For example, the cold head of the pulse tube is connected via copper braids to the 50 Kelvin and 3 Kelvin plate instead of a rigid connection. Furthermore, the still plate is suspended via springs from the 3 Kelvin plate to form a mass spring system with a cut-off frequency of approximately 2 Hz of which the motion is damped by Eddy current dampers. A more detailed overview is presented in the work of den Haan et al. [129]. Although these modifications are a major improvement, additional isolation between the mixing chamber plate and the experimental set-up is needed. Based on the work of K. Heeck [130], we will discuss in this section the design of a mechanical low-pass filter.

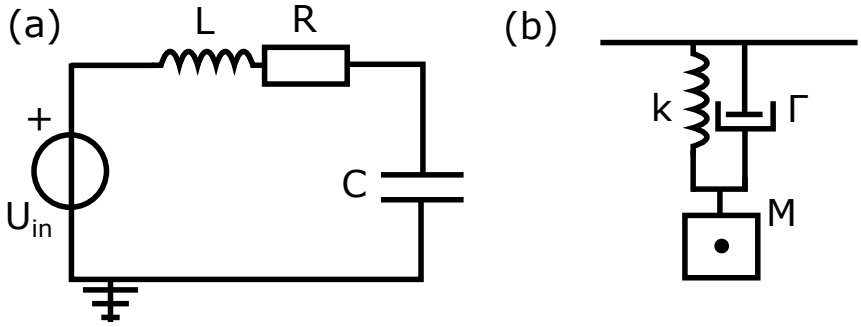

Figure 10.1: The response of the LCR circuit in (a) and the damped harmonic oscillator in (b) can both be described by a differential equation of the same form.

10.1.1 Correspondence between electrical and mechanical networks

Filters are common in electrical circuits, making them a natural place to start. Additionally, there is a correspondence between electrical circuits, such as the LCR circuit shown in Fig. 10.1(a), and mechanical structures, such as the damped harmonic oscillator in Fig. 10.1(b). We will illustrate this correspondence with a simple example. Using Kirchoff's voltage law, the following differential equation is obtained for the circuit in Fig. 10.1(a):

$$L\frac{d^2q}{dt^2} + R\frac{dq}{dt} + \frac{q}{C} = U_{in} \tag{10.1}$$

in which L is the inductance, R the resistance, C the capacitance, q the charge and U_{in} the input voltage. Using Newton's laws, the following equation of motion is obtained for the damped harmonic oscillator in Fig. 10.1(b):

$$M\frac{d^2x}{dt^2} + M\Gamma\frac{dx}{dt} + kx = 0 \tag{10.2}$$

in which M is the mass, Γ the damping rate, k the spring constant and x the displacement. When comparing Eqs. (10.1) and (10.2) one can see that they are both second-order differential equations. Furthermore, one can link equivalent components together: mass and inductance, damping rate and resistance, and spring constant and capacitance.

Kirchoff's voltage law states that the sum of the electrical potential differences in any closed loop is zero. This is an example of a loop or maze equation. Kirchoff's current law states that the sum of all currents flowing to and from a node add up to zero. This is an example of a node equation. Equation (10.1) is derived via a maze equation, while Eq. (10.2) adds all forces at the center of mass M. Equation (10.2) is therefore a node equation. Since node equations in electrical circuits relate to currents, we can link an electrical current to a mechanical force. Finally, since both the velocity and the voltage have a gauge freedom (i.e. offsets can be added freely to them without changing the physics) we see that they are analogous and thus we can

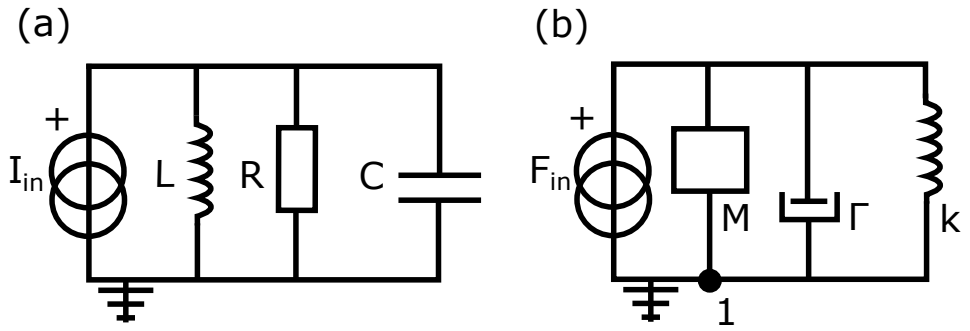

Figure 10.2: (a) The dual of the series LCR circuit is a parallel LCR circuit. (b) The mechanical circuit diagram of a damped harmonic oscillator.

connect voltage to velocity.[1]

With the correspondence in place, we can ask the following question: can we find the circuit diagram of the mechanical structure in Fig. 10.1(b), using the LCR circuit in (a) as a starting point? If we take the dual network [131] of the LCR circuit, the voltage source becomes a current source and all elements in series will now be in parallel.[2] Figure 10.2(a) shows this dual circuit. Note that the series LCR circuit of Fig. 10.1(a) describes a band-pass filter, while the dual circuit, a parallel LCR circuit, is a band-stop filter. The dual transformation has inverted all properties of the original network. If we now replace all electrical components with their mechanical counterparts, we obtain the circuit shown in Fig. 10.2(b). Applying the node equation to the node indicated with 1 in Fig. 10.2(b), we obtain the following equation:

$$M\frac{d^2x}{dt^2} + M\Gamma\frac{dx}{dt} + kx = F_{in} \tag{10.3}$$

which is precisely the equation of motion describing a damped harmonic oscillator. Although the schematic overview shown in Fig. 10.1(b) and the mechanical circuit diagram of Fig. 10.2(b) may not look the same, they are both described by the same differential equation and are therefore equivalent representations of a damped harmonic oscillator.

The mechanical circuit diagram has some interesting properties. For example, it makes sense that a damper and spring have two connections on either side, just as their electrical counterparts. But what does it mean that the mass M has two connections as well? Velocity has now taken the role of voltage. As such, the velocity must be expressed with respect to some reference, in this case the coordinate origin. This coordinate origin is the same for all the velocities of the masses.[3] The most conve-

[1] Not only velocity but also position has a gauge freedom. It is, however, convenient to have velocity correspond to voltage. As we will see in the next paragraphs.

[2] Additionally, one writes down the conductance of each element instead of the impedance, when transforming to the dual network, see the work of Tellegen [131] for a rigorous treatment.

[3] If this is not the case, we have a mechanical circuit that connects different inertial reference frames together. Since the velocity of each frame does not need to be the same, the circuit can literally be pulled apart.

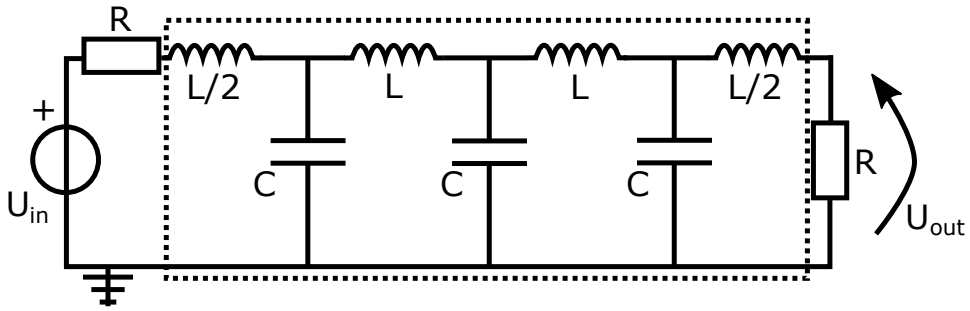

Figure 10.3: Circuit diagram of a third order electrical low-pass filter, shown in the dashed box. This is the starting point for designing the mechanical filter.

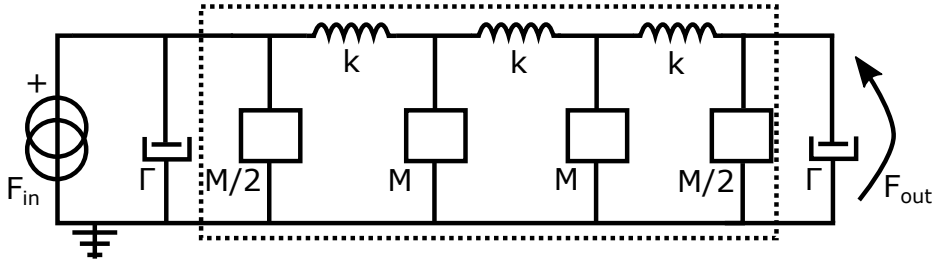

Figure 10.4: Circuit diagram of the ideal mechanical low-pass filter derived from the electrical equivalent circuit shown in Fig. 10.3.

nient reference is therefore to connect each mass to ground. Although any electrical circuit has a mechanical equivalent, only mechanical circuits with the masses connected to ground can be physically realized. Therefore the original electrical circuit must have the inductors on the outer contours of the diagram.

We have found the equivalent mechanical circuit diagram by starting with an LCR circuit, writing down the dual circuit and interchanging electrical for mechanical components. The original LCR circuit acts as an electrical band-pass filter, while the damped harmonic oscillator can be viewed as a mechanical band-pass filter. To design a mechanical low-pass filter, we can thus use an electrical low-pass filter of choice as a blue-print for the mechanical low-pass filter, as we will show in the next section.

10.1.2 Mechanical low-pass filter

The most simple example of an electrical low-pass filter is perhaps the wave filter (constant-k filter) [132], in which identical sections make up a ladder structure. A third order electrical low-pass filter, see Figure 10.3, is chosen as a starting point. Higher order filters are of course possible, at the expense of a larger structure. A third order filter is therefore a compromise between performance and size.

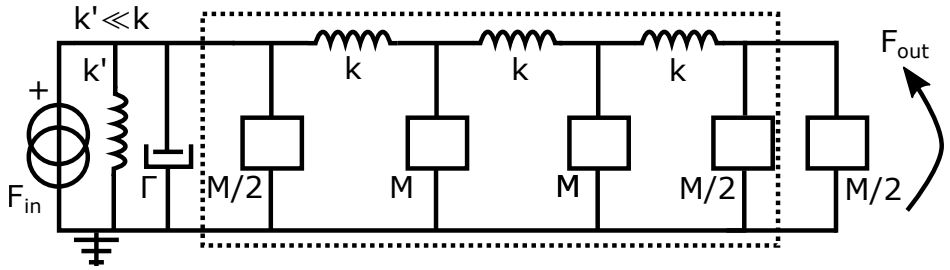

Figure 10.5: The final mechanical low-pass filter. Compared to the ideal low-pass filter in Fig. 10.4 the damper at the output is replaced with an additional mass, and the input has as an additional weak spring in parallel to carry DC forces.

If we now follow the method outlined in the previous section, we can write down the dual of the circuit in Fig. 10.3 and interchange the electrical components for their mechanical counterparts. The resulting circuit is shown in Fig. 10.4. We can already see that this mechanical filter can be physically realized, because each mass is connected to ground. With this in mind, one can also see that the damper at the output is impossible to construct, because the damper should also be referenced to the coordinate origin. This means that the damper will largely bypass the filter. No damper at the end means that reflections in the filter itself will increase the velocity at the output above the corner frequency of the filter. Numerical simulations show that this problem can be reduced by adding a mass $M/2$ to the output.

At the input a small adjustment is also needed. Suppose a DC force, for example the gravitational force acting on the optical set-up connected to the filter, is applied to the output of the filter shown in Fig. 10.4. Because this DC force is not resonant with any closed loop of the circuit, no force is generated to counteract the applied DC force. Therefore, the DC force is directly transmitted to the damper at the input. The response of the damper is to continuously expand, therefore the damper can not carry a DC force. This problem can be solved by adding a weak spring, with a spring constant much smaller than the spring constant of the interconnecting springs, parallel to the damper. The final diagram of the mechanical low-pass filter is shown in Fig. 10.5.

With the diagram of the filter explained, we turn to the characteristics of the filter. To calculate the corner frequency, we make use of the theory developed for wave filters by Campbell [132]. The corner frequency of the filter shown in Fig. 10.5 is given by $f_0 = \frac{1}{\pi}\sqrt{k/m}$. Because the optical set-up shown in chapter 2 has a mass of 3.5 kg, it makes sense to choose the masses of the filter to be of that order. Although we would like to have the corner frequency to be as small as possible and therefore have very weak springs, the filter must still be able to carry weight of the set-up. This naturally limits the spring constant of the springs. We have chosen a mass m of 2 kg and a spring constant k of 50 kN/m, resulting in a corner frequency of $f_0 = 50$ Hz.

The only thing missing is the full transfer function of the mechanical filter. Figure 10.6(a) shows a schematic overview of the filter, based on the circuit diagram of Fig.

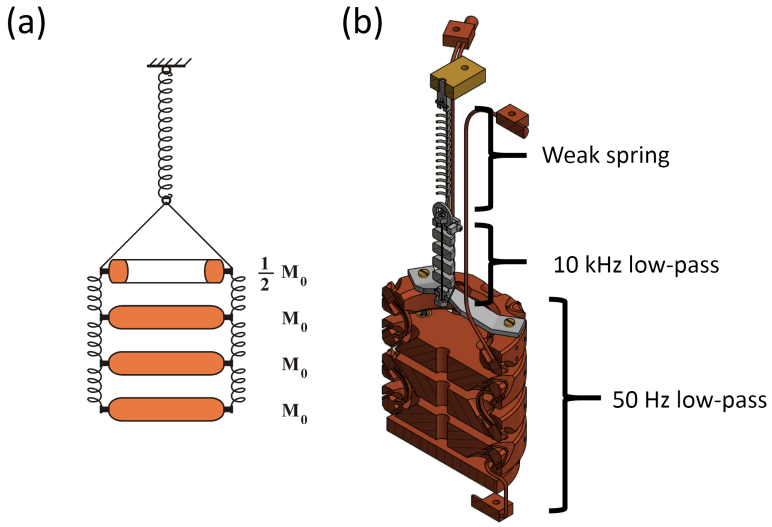

Figure 10.6: (a) Schematic overview of the third order mechanical low-pass filter based on the circuit diagram of Fig. 10.5. Note that the damper at the input is missing. (b) The final vibration isolation system, designed by K. Heeck and constructed by H. van der Meer, as used in the cryostat. Besides the mechanical filter with a corner frequency of 50 Hz, an additional low-pass filter at 10 kHz is added to reduce vibrations generated by the pulse tube's control current.

10.5. The damper at the input is not shown. The mechanical filter is nothing more than a coupled mass-spring system. Using Newton's laws, the full transfer function can be calculated. The final vibration isolation system is shown in Fig. 10.6(b). An additional low-pass filter at 10 kHz is also added to reduce mechanical noise in the cold head at 26 kHz, generated by the control current of the pulse tube. This filter is designed following the same principles as outlined above.

At the time of writing, a cryogenically compatible damper was still in development, therefore the vibration isolation system was operated without the damper. The performance of each filter was separately tested. For the 10 kHz filter as well as the 50 Hz filter, the position of each mechanical resonance was verified experimentally. Additionally, the transfer function of the 50 Hz filter was also measured at room temperature by applying a force excitation with constant amplitude via a voice coil attached to the first mass while measuring the response using a geophone attached to the final mass. Although this method of excitation only approximates a constant force excitation, it does provide a reasonable indication of the performance of the isolation stage. The results are shown in Fig. 10.7 together with the expected transfer function [130]. Although there are some discrepancies, the measurement matches the expected transfer function quite well. In particular, above 100 Hz more than 100 dB of isolation is achieved.

Four distinctive resonances are visible in Fig. 10.7, corresponding to the different

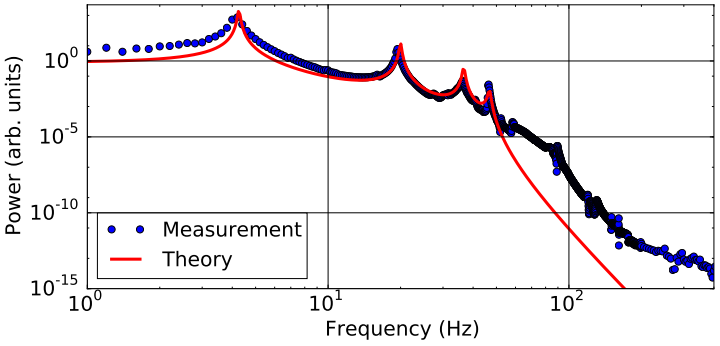

Figure 10.7: The mechanical transfer function as measured at room temperature for the 50 Hz filter, together with the theoretical prediction.

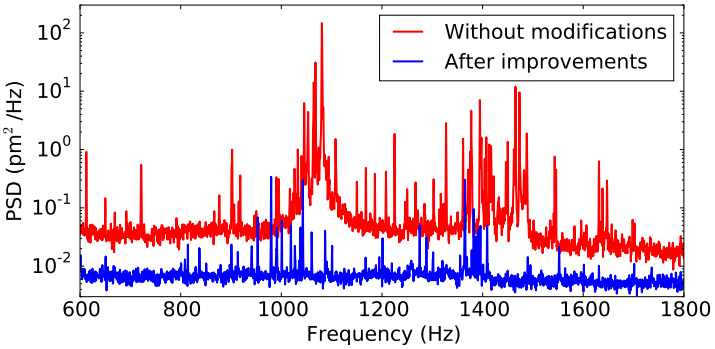

Figure 10.8: Mechanical displacement spectra as measured via the optical cavity at 100 mK. Red: the noise with a single stage mass-spring system and no modification to the cryostat. Blue: the remaining noise after lifting the pulse tube, suspending the still and using the vibration isolation system shown in Fig. 10.6(b).

modes of the mass-spring system itself. These can be suppressed by adding the mechanical damper. These additional resonances are however not an issue. Because the laser is actively locked to the cavity resonance, low frequency vibrations can be compensated for. The real problem was the internal mechanical modes of the optical set-up. These occur roughly at 1 kHz, the region in which the isolation system of Fig. 10.6 should perform optimally.

In Fig. 10.8 mechanical displacement spectra as measured via the optical cavity at 100 mK are shown. Without any modifications to the cryostat and using only a single stage mass-spring system, significant noise is visible between 1 and 1.6 kHz, as is indicated in red. After the modifications to the cryostat and using the isolation stage shown in Fig. 10.6(b), the noise has significantly reduced, as is shown in blue. The next section will show that with this isolation stage, sensitive optical experiments at cryogenic temperatures are possible.

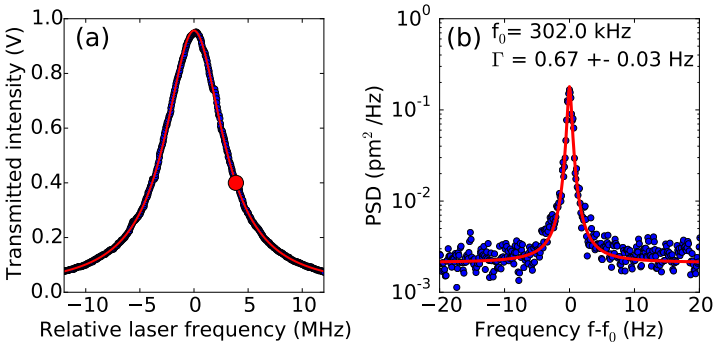

Figure 10.9: (a) Cavity resonance for the low finesse cavity created by using a 950 nm laser. (b) Power spectrum of the thermal motion measured via a side-of-fringe lock to the low finesse cavity. The red dot in (a) indicates the laser frequency that was used to measure the spectrum of (b).

10.2 Optical side-band cooling at cryogenic temperatures

Cooling down the cryostat occurs in two stages, first the cryostat cools to a base temperature of 5.7 Kelvin using the pulse tube cooler. During this stage, the active feedback demonstrated in the previous chapter is used to damp the motion of the outer resonator, while the PiezoKnob motors are used to actively keep the cavity aligned. When the base temperature is reached, all motors are shorted and the active feedback is turned off. The next step is to turn on the dilution refrigerator to reach mK temperatures. First we will report on measurements performed at 5.7 Kelvin. The cooling power of the cryostat at this temperature is significantly higher than at mK temperatures, so the lasers are not likely to heat up the set-up. After demonstrating stable operation of the optomechanical set-up at 5.7 Kelvin, the base temperature is lowered via the dilution refrigerator to see if the mechanical mode can be cooled even further.

10.2.1 Measurements at 5.7 Kelvin

First, we need verification of the mechanical mode temperature to confirm that the sample has thermalized properly. To ensure that the optical read-out does not modify the mechanical motion of the resonator via the optomechanical interaction, a laser wavelength of 950 nm is used, well outside the coating specifications of the DBR mirrors. In Fig. 10.9(a) the cavity resonance is shown together with a Lorentzian fit. The linewidth of the resonance is 6.5 MHz, resulting in a finesse of about 460. Via a side-of-fringe lock (see chapter 2) at a detuning indicated by the red dot in Fig. 10.9(a), the thermal motion of the resonator is measured. Because the finesse is low, the laser is far detuned and low laser power is used, optomechanical cooling and damping should not occur. This is verified by switching from positive to negative detunings and observing no change in the measured linewidth. Therefore this method is able

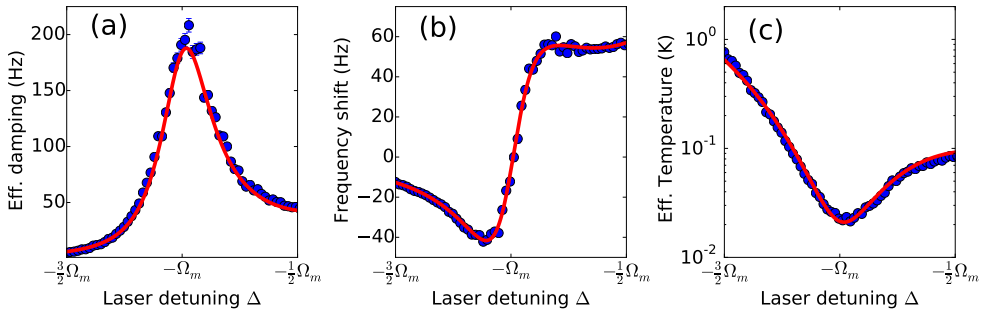

Figure 10.10: The blue data-points are obtained via a Loretzian fit to the mechanical power spectra obtained from the PDH probe signal. The effective temperature is obtained from the integrated displacement power spectral density. The red curves are the result of a simultaneous fit to all three data-sets with only the optical linewidth and input power as free parameters.

to measure the intrinsic mechanical linewidth. Figure 10.9(b) shows the observed thermal motion. At 5.7 Kelvin we find a line-width of 0.67±0.03 Hz at a frequency of 302 kHz.

Typically the power spectrum is measured in units of $\mathrm{V}^2_{\mathrm{rms}}/\mathrm{Hz}$. From the optical resonance shown in Fig. 10.9(a) we can obtain the slope, in units of V/Hz at the specific detuning from the Lorentzian fit. Via the optical frequency shift per displacement $G = \frac{\omega_{cav}}{L}$, we can obtain a conversion factor in units of V/m. Via this conversion factor we can transform the scale of the measured power spectrum to m^2/Hz as is shown in Fig. 10.9(b). The area of the Lorenztian gives directly the displacement $\langle x(t)^2 \rangle$ of the mechanical resonator in the correct units. The mode temperature can be calculated via the equipartition theorem

$$T_{mode} = \frac{\langle x(t)^2 \rangle m \Omega_m^2}{k_b} \tag{10.4}$$

and using a mass of $m = 140$ ng obtained via COMSOL. We find a mode temperature of 5.7 ± 0.3 Kelvin, indicating that the mechanical mode is indeed thermalized to the base temperature of the cryostat. This method has been verified separately at room temperature as well, where the mode temperature is known.

To demonstrate the stability of the optical system at low temperatures, we use the method outlined in chapter 5 to perform optical side-band cooling. As a function of laser detuning we measure the mechanical displacement spectrum. By fitting the noise spectrum with a Lorentzian, we directly obtain the mechanical linewidth and frequency shift. The area of the Lorentzian is propertional to the effective temperature. As discussed in chapter 5, we use a relative calibration to scale this area to an effective temperature. As shown by the side-of-fringe lock in Fig. 10.9, the resonator is thermalized to the base temperature of the cryostat. Consequently, if we measure via the Pound-Drever-Hall (PDH) method the displacement of the resonator, we know that a measured linewidth of 0.67 Hz should correspond to a mode

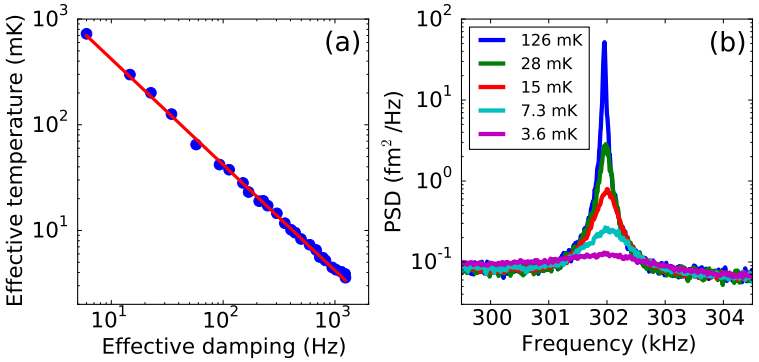

Figure 10.11: At a fixed laser detuning of $\Delta = -\Omega_m$ the intensity of the pump laser is varied. (a) The effective linewidth and effective temperature show the expected behavior indicated by the red line. (b) Selection of mechanical displacement spectra, showing that the spectra are very clean.

temperature of 5.7 Kelvin. We have, however, noticed that the mode temperature increases with read-out laser power. For typical laser powers the mode temperature has increased from 5.7 to 6.5 Kelvin. The thermalization of the resonator is investigated in more detail in the next section.

The results are shown in Fig. 10.10 for an hour long, fully automated measurement. From the fitted red line, a value of 82±2 kHz is obtained for the optical linewidth, showing that our system is side-band resolved. Furthermore, the excellent agreement between theory and experiment demonstrates that we have created a stable platform for sensitive optical experiments at low temperatures.

Figure 10.11 shows the results of side-band cooling when the cooling laser is fixed at $\Delta = -\Omega_m$ and the power is varied. The results follow theory nicely, as indicated by the red line. In Fig. 10.11(b) some of the mechanical displacement spectra are shown. Note that the scale on the y-axis is obtained by comparing the measurements with the calibrated side-of-fringe method of Fig. 10.9. At the highest laser powers an effective mechanical mode temperature of 3.6 $\pm$ 0.13 mK is achieved. As can be see from Fig. 10.11(b), the mechanical spectra are very clean, thanks to the vibration isolation system and the nested resonator. When increasing the cooling laser power even further, the mechanical spectrum can no longer be distinguished from the noise floor anymore.

At low read-out laser powers, the noise floor is limited by shot noise. Increasing the laser power decreases the noise floor, but only down to the value shown in Fig. 10.11(b). A quick calculation [38] shows we are at least two orders of magnitude away from the the shot noise limit. This suggests that additional technical noise dominates at these read-out powers. Furthermore, the noise floor has a definite slope. This becomes clearer when looking at the full power spectrum of the PDH error signal, as shown in Fig. 10.12. Up to 20 kHz the effects of the laser feedback are clearly visible, after which the noise floor gradually decreases. A decrease in noise floor with frequency suggest $1/f$ type noise, however, careful investigation

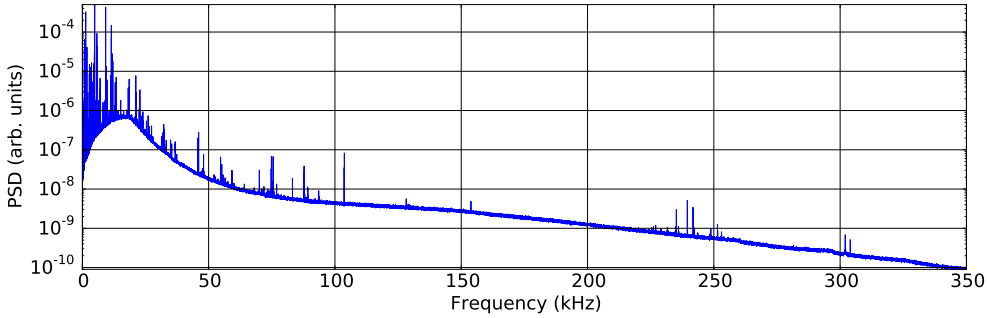

Figure 10.12: Full power spectrum of the PDH error signal. A clear downward slope is visible towards higher frequencies.

is needed. For example, the cavity itself acts as a low-pass filter, with the optical line-width κ as the corner frequency. This would, however, not explain the limit to the read-out noise.

Besides the read-out noise floor, we are also limited by the intrinsic Q-factor of the mechanical resonator. A higher Q-factor will directly result in a lower effective temperature, assuming all other parameters are fixed [97]. In the next section, the temperature of the cryostat is lowered with the dilution refrigerator. The hypothesis is that the lower base temperature together with optical cooling lead to a significantly lower effective mode temperature of the mechanical resonator than presented here for the base temperature of 5.7 K.

10.2.2 Thermalization of the trampoline resonator

Optical cooling from a base temperature of 5.7 Kelvin has resulted in an effective mode temperature of 3.6 mK. When lowering the base temperature to 100 mK, effective mode temperatures below 1 mK should be possible. Because the side-of-fringe method has limited sensitivity, the spectra measured at 5.7 Kelvin via the PDH technique, which is much more sensitive, can serve as a reference for determining the effective mode temperature at lower baser temperatures. This does require a method to monitor the read-out sensitivity to be able to correct for any change in the read-out when cooling down from 5.7 K to mK temperatures. Therefore, a calibration tone at 304 kHz, generated by the same electric-optical modulator used for the Pound-Drever-Hall (PDH) technique, is added to the read-out laser.

Figure 10.13 shows the results of side-band cooling for a fixed laser detuning of $\Delta = -\Omega_m$ starting from a base temperature of 300 mK as measured with a RuO2 thermometer. The effective linewidth increases with laser power, as is shown in Fig. 10.13(a). The effective temperature, however, does not continuously decrease with laser power. Furthermore, the lowest effective mode temperature that is achieved is 3.09 ± 0.07 mK, only slightly lower than the measurements performed at 5.7 K.

There are several possibilities why a lower base temperature does not lead to a significantly lower effective temperature. For example, the mechanical Q-factor

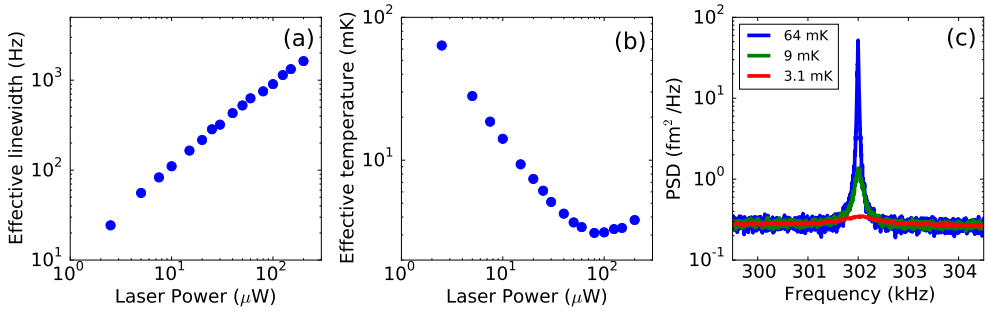

Figure 10.13: At a base temperature of 300 mK the laser detuning is fixed at $\Delta = -\Omega_m$ and the intensity of the pump laser is varied. (a) Effective line-width as function of laser power of the cooling beam. (b) Effective temperature as function of laser power of the cooling beam. (c) Selection of mechanical displacement spectra.

could have decreased when cooling down to mK temperatures. Another explanation is that the mechanical mode thermalizes poorly. Both explanations can be investigated by using the side-of-fringe technique shown in Fig. 10.9 to determine the intrinsic mechanical linewidth and the mode temperature.

The results in Fig. 10.14(a) show that the mechanical linewidth is roughly constant when the setpoint of the side-of-fringe lock is varied. The setpoint is the transmitted intensity to which the laser frequency is stabilized. The mode temperature increases significantly with increasing setpoint, as is shown in Fig 10.14(b). The temperature of the optical set-up was 200 mK during the entire measurement run and the measurements were performed from high to low setpoint. A higher setpoint means a larger transmitted intensity through the trampoline resonator, this suggests that heating of the mechanical mode due to optical absorption is the cause of the increased mode temperature. Another explanation is that the laser noise at the mechanical frequency of the resonator causes the mode temperature to increase. Laser noise can be ruled out as the cause of the increased mode temperature by repeating the experiment with a different laser at 1064 nm locked to the cavity resonance via the PDH technique. In Fig. 10.15 the mode temperature of the resonator is shown as function of read-out laser power for a base temperature of 5.7 K and 200 mK. The increase in read-out sensitivity with laser power is taken into account via the additional calibration tone. The read-out power displayed on the horizontal axis is the power in the optical fiber towards the optical set-up. At 5.7 K the read-out laser heats up the mechanical mode with approximately 1 K. The mode temperature increases even more at 200 mK, reaching a mode temperature of almost 4 K.

The increase in mode temperature with laser power is observed with two different lasers and two different measurement techniques. Also, at 200 mK the increase in temperature is larger for the same input power compared to measurements at 5.7 K. All these results can be explained by heating of the DBR mirror due to optical absorption and subsequently poor heat conduction through the silicon nitride arms. If we assume thermal equilibrium for the mechanical mode temperature when the

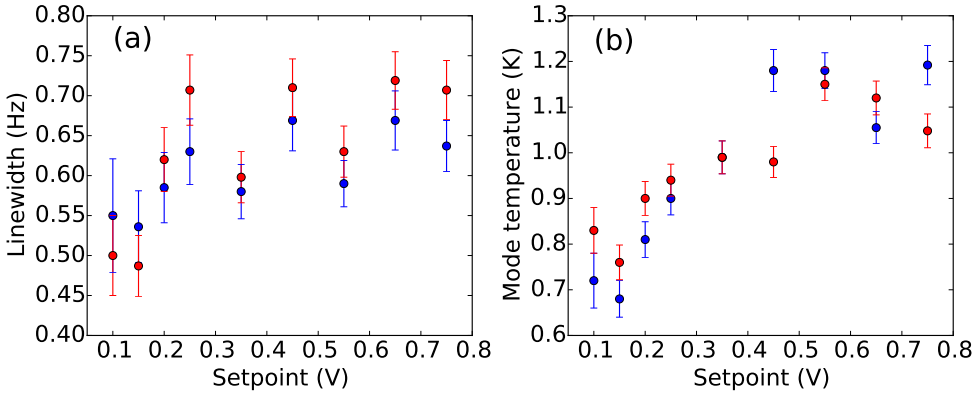

Figure 10.14: Via the side-of-fringe lock to a low finesse cavity, the mechanical linewidth shown in (a) and the mode temperature shown in (b) are obtained as a function of setpoint at a base temperature of 200 mK. Each setpoint is measured both on the blue side (blue points) and on the red side (red points) of the cavity resonance.

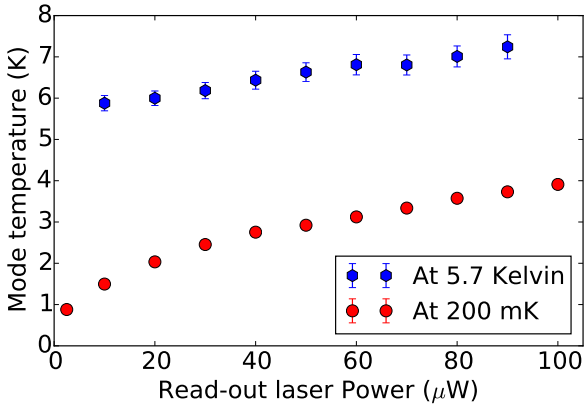

Figure 10.15: Comparison of the mode temperature as function of read-out laser power both at 5.7 K and approximately 200 mK.

laser is on, the heat conduction can be described by Fourier's law:

$$\frac{P_{abs}}{A} = -k\frac{dT}{dx} \tag{10.5}$$

where P_{abs} is the absorbed optical power, A is the cross-section perpendicular to the heat flow, k is the heat conductivity, and dT/dx the temperature gradient. Fourier's law might not be entirely valid for these small structures, but it will give a rough estimate. We can rewrite Eq. (10.5) in the following way to find the temperature difference between the DBR mirror and the support of the silicon nitride arms:

$$\Delta T = \frac{1}{4}\frac{P_{abs}\Delta x}{Ak} \tag{10.6}$$

where the factor $1/4$ accounts for the four arms of the resonator and Δx is the length of one arm. One silicon nitride arm has the following dimensions: $\Delta x = 175$ μm, $A = w \times t$ with a width $w = 50$ μm and thickness $t = 400$ nm. Zink and Hellman have investigated the thermal conductivity of low-stress amorphous silicon nitride membranes [133]. Although we use high stress silicon nitride, we can use their value of $k = 0.1$ W/(K m) at 5 K as an estimate.

For 1 μW of optical read-out power in the fiber, we can estimate how much light leaks out of the cavity. With a mode-matching efficiency of 0.33 and a cavity coupling $\kappa_{ex}/\kappa = 0.15$, we estimate that 280 nW leaks out of the cavity through the trampoline resonator for 1 μW of optical power in the fiber. Suppose now that the DBR mirror on the trampoline resonator has 100 ppm transmission. The 280 nW of transmitted light corresponds to 100 ppm of the circulating power. Assuming 0.5 ppm of optical absorption in the DBR, this then corresponds to 1.4 nW of absorbed optical power. Of course, the silicon nitride layer underneath the DBR mirror can also absorb light. A quick estimate using the absorption coefficient of silicon nitride shows that this is at least an order of magnitude smaller than the absorption in the DBR mirror.

From Fig. 10.15 we see that 80 μW of read-out power at 5.7 K warms up the mode temperature with approximately 1 K. A read-out power of 80 μW corresponds to an estimated absorbed power of 112 nW. Using Eq. (10.6) this results in a temperature difference of 2.45 Kelvin. Although we have made several assumptions and guesses, (we have, for example, not taken the outer resonator into account) the fact that we find roughly the same value makes heating due to optical absorption plausible.

The thermal conductivity of silicon nitride at even lower temperatures is not well known, but generally the heat conductivity decreases when the temperature is lowered even further. This would explain the larger increase in mode temperature at 200 mK compared to the measurements at 5.7 K. Finally, heating of mechanical resonators due to optical absorption has been reported in literature as well. Experiments involving a silicon cantilever cooled to 300 mK show that the mechanical mode temperature increases significantly when only 70 nW of laser power is used for the optical read-out [134].

From Fig. 10.15 it is clear that there might be an optimal read-out power when performing an optical cooling experiment. However, this does not yet take heating due to the cooling beam into account. The measurements presented in Fig. 10.13 are performed with a read-out laser power of 20 μW. As shown in Fig. 10.13, the effective

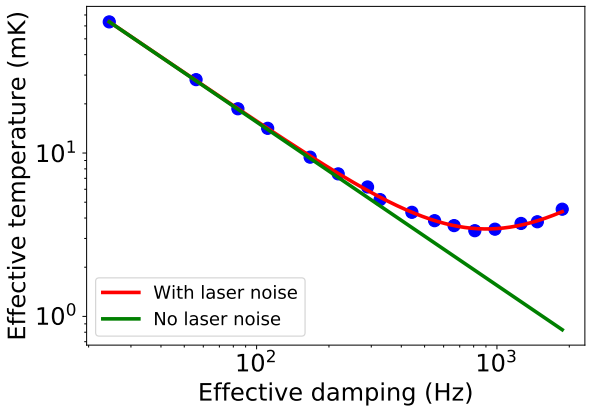

Figure 10.16: Effective mode temperature as function of effective damping. In red the fit is shown with the presence of classical laser noise, while in green the expected effective temperature is shown.

mode temperature increases again for high cooling beam powers, suggesting that also optical absorption of the pump beam occurs. The pump beam is placed at $\Delta = -\Omega_m$, so only 1.8 % of the pump beam is transmitted through the cavity compared to a detuning of $\Delta = 0$. Even with the high cooling laser powers used in 10.13, this fraction is simply too small to explain the increase in effective temperature shown in Fig. 10.13(b).

An alternative explanation is heating due to classical laser noise. As discussed in chapter 2, the effective temperature of the resonator can be written as

$$T_{\mathit{eff}} = \frac{T_{env}\Gamma_m + T_{optical}\Gamma_{opt}}{\Gamma_{opt} + \Gamma_m}. \tag{10.7}$$

Jayich et al. have shown how classical laser noise (amplitude and phase) affects the effective temperature [135]. We will not repeat the derivation, but using their assumption that the laser noise is proportional to the laser power, we can write Eq. (10.7) as follows:

$$T_{\mathit{eff}} = \frac{T_{env}\Gamma_m + T_{optical}(P_{laser})\Gamma_{opt}}{\Gamma_{opt} + \Gamma_m} \tag{10.8}$$

with $T_{optical}(P_{laser}) = \alpha P_{laser}$ this becomes

$$T_{\mathit{eff}} = \frac{T_{env}\Gamma_m + \alpha P_{laser}\Gamma_{opt}}{\Gamma_{opt} + \Gamma_m} \tag{10.9}$$

We can check the hypothesis of classical laser noise by using Eq. (10.9) to fit the data of Fig. 10.13(b). The results are shown in Fig.10.16. The data fit the theory well, indicating that classical laser noise is the problem. This might also explain why the noise floor of the read-out of the mechanical motion is not shot-noise limited. The solution would be to implement a filter cavity to reduce the classical laser noise [135].

The issue of optical absorption in DBR mirror of the trampoline resonator might be more difficult to solve. An alternative to trampoline resonators would be to use thin silicon nitride membranes, which can be used in a membrane-in-the-middle configuration. Because the membrane is placed at a node of the cavity field and the membrane is very thin (50 nm or less), optical absorption might not have such a big impact. Also, the mechanical Q-factor of these membranes is orders of magnitude larger. Both should help with achieving the quantum mechanical ground-state via optical side-band cooling. The next chapter discusses in more detail the advantages of membrane resonators.

Acknowledgment

We would like to thank Martin de Wit and Gesa Welker for operating the dilution refrigerator. We also thank Yasmine Sfendla for useful discussions.